Near-threshold femtosecond laser fabrication of one-dimensional subwavelength nanogratings on a graphite surface

E. V. Golosov,[1] A. A. Ionin,[2] Yu. R. Kolobov,[1] S. I. Kudryashov,[2,*] A. E. Ligachev,[3] S. V. Makarov,[2,4] Yu. N. Novoselov,[2] L. V. Seleznev,[2] D. V. Sinitsyn,[2] and A. R. Sharipov[2,5]

[1]*Belgorod State University, Belgorod, Russia*

[2]*P. N. Lebedev Physical Institute, Russian Academy of Sciences, Moscow, Russia*

[3]*A. M. Prokhorov General Physics Institute, Russian Academy of Sciences, Moscow, Russia*

[4]*National Research Nuclear University "MEPhI," Moscow, Russia*

[5]*Moscow Institute of Physics and Technology (State University) "MFTI," Moscow, Russia*

(Received 11 October 2010; revised manuscript received 18 November 2010; published 14 March 2011)

Superimposed one-dimensional quasiperiodic gratings with multiple periods $\Lambda \approx 110$–800 nm well below or comparable to the pump laser wavelength of 744 nm, and ridge orientations perpendicular to the linear polarization of infrared femtosecond laser pulses, were fabricated after multiple near-threshold laser shots on a planar surface of quasimonocrystalline graphite in ambient air. The broad range of the grating periods corresponds to the large number of spatial Fourier harmonics of the final nanorelief (up to $m = 7$th order, $\Lambda_m \approx 800$ nm$/m =$ 110–800 nm), qualitatively representing the nonsinusoidal profile of the laser-induced intermediate surface relief (the set of periodic, broadly spaced narrow nanotrenches), which provides the corresponding multiangle diffraction of the incident femtosecond laser pulses. Experimental measurements and modeling of the transient optical constants of the photoexcited graphite justify the excitation, at the first stage, of the first-order ($\Lambda_1 \approx 800$ nm) surface plasmon-polaritonic (SPP) wave on the photo-excited initial planar graphite surface becoming metallic via photo-generation of dense electron hole plasma ($\sim 10^{21}$ cm^{-3}). Such an SPP wave provides intermediate nanorelief in the form of the nonsinusoidal surface grating via its interference with the incident laser wave, resulting under near-threshold laser irradiation conditions in the highly localized surface ablation of the material in the interference maxima. During the next stage, the multiperiod subwavelength nanogratings develop through the multiangle diffraction of the multiple incident laser pulses on the intermediate nonsinusoidal surface grating.

DOI: 10.1103/PhysRevB.83.115426 PACS number(s): 79.20.Ds, 81.07.−b, 81.16.−c

I. INTRODUCTION

During the past decade, the possibility of multishot femtosecond (fs) laser fabrication of subwavelength one-dimensional (1D) surface gratings (suboptical wavelength periods $\Lambda = 70$–400 nm $\leqslant \lambda_{las}$, where $\lambda_{las} \approx 800$ nm is the typical fs-laser pump wavelength) was demonstrated for very diverse materials: metals, semiconductors, and dielectrics.[1–14] The underlying fabrication mechanism widely accepted since the early 1980s is related to a near-field scattering (diffraction) of incident fs-laser pulses on nano- and microscale intrinsic or extrinsic surface roughness. Some angular components of the diffracted wave, which propagate along the initial unstructured, rather flat surfaces of such fs-laser excited materials, may excite on them surface electromagnetic (EM) waves [in other words, surface plasmon-polaritons (SPP) or just surface plasmons] with the laser frequency ω_{las} and specific in-plane wave vector $\boldsymbol{k}_{||}$, which is collinear to the laser polarization vector $\boldsymbol{e}$. It is assumed that the subsequent constructive interference between the in-plane component of the SPP electric field and the in-plane component of the directly incident, nondiffracting fs-laser wave provides the resulting 1D periodic distribution of energy density and ablative modification of the surface relief once the ablation threshold of the host material is locally exceeded.[13–15] The resulting *single* surface nanograting is of the predicted *single near-wavelength* spatial period $\Lambda \approx \lambda_{las}/\eta$ (where the scaling factor $\eta \sim 1$),[15] rather than the observed much smaller *subwavelength* periods.

To overcome this obstacle in explaining fs-laser fabrication of 1D subwavelength surface nanogratings,[1–13] sometimes including simultaneously also higher—typically second—harmonics of such near-wavelength nanogratings,[1,4] different viewpoints regarding the initial laser-matter interaction step and the subsequent evolution of the excited SPP waves have appeared. First, surface generation of in-plane optical second and higher harmonics in a reflection mode was suggested[1] accounting for potential high magnitudes of surface optical nonlinearities. Alternatively, a few colliding SPP waves were suggested to result in specific subwavelength surface nanogratings with wave numbers $2^n|\boldsymbol{k}_{||}|$.[4,14] However, in the absence of direct clarifying experimental evidence in favor of these hypotheses, the actual mechanism underlying fs-laser fabrication of 1D sub-wavelength surface nanogratings is still far from being clearly inderstood.

With a little clear knowledge achieved so far regarding the SPP wave excitation and interaction with the laser wave on the transiently excited material surface with its optical constants, considerably modified by the same fs-laser pump pulse, much less attention has been paid to other subsequent, intermediate steps of such cumulative nanograting fabrication. The latter important steps are (i) formation of the intermediate periodic nanograting relief with the single near-wavelength intertrench distance, if the local laser energy density deposited in the laser-SPP wave interference maxima exceeds the ablation threshold one, and (ii) ongoing diffraction of the incident laser wave on the intermediate near-wavelength, single-period nanograting

(typically with a nonsinusoidal profile), resulting in a number of in-plane diffracted angular components.[16] These angular components couple to the surface in the form of multiple SPP waves with the same frequency ω_{las} and different m-folded wave numbers ($m|\boldsymbol{k}_{||}|, m = 1,2,3,\ldots$) and may be imprinted in each intertrench space in the form of higher nanorelief harmonics ($\Lambda_m \approx \lambda_{las}/\eta m$) (Ref. 17) via their constructive interference with the incident laser wave. Hence, in lieu of these theoretical predictions,[17] the fabrication mechanism of subwavelength surface gratings should be more thoroughly studied also in relation to the formation of the intermediate nanorelief and the ongoing diffraction effects.

In this work, we report on multishot near-threshold fs-laser fabrication in ambient air on a flat graphite surface of subwavelength 1D nanogratings with periods $\Lambda_m \approx$ 800 nm$/m$ = 110–800 nm, corresponding to a large series of superimposed surface nanorelief spatial harmonics up to $m = 7$th order. Optical reflection studies were conducted to obtain transient optical constants of the photoexcited material and then to evaluate the fs-laser fluence threshold for SPP excitation, the lower bound for the surface nanostructuring threshold, and the maximal (first-order) period of the initial laser-SPP interference surface patterns. Finally, the observed well-developed surface nanorelief with a large number of superimposed higher spatial harmonics (subwavelegnth nanogratings) qualitatively represented in the SEM images was used as a qualitative illustration for a two-stage fabrication process, involving the initial near-threshold formation of the intermediate near-wavelength, single-period nonsinusoidal surface nanograting of equidistant trenches, and the subsequent multiangle diffraction of the incident laser pulses on the grating yielded in the multiple spatial harmonics of the surface nanorelief.

II. EXPERIMENTAL SETUP, SAMPLES, AND PROCEDURES

In our experiments, we used a Ti:sapphire laser system (Avesta Project Ltd.) providing regeneratively and multipass-amplified 744-nm laser pulses with pulse width $\tau_{las} \approx 70$ fs and maximum pulse energy E_{max} about 6 mJ with Gaussian radial fluence distribution $F(r) = (E/\pi\sigma^2)\exp(-r^2/\sigma^2)$ in TEM_{00} mode.[13] The laser pulses were weakly focused at normal incidence into a 1-mm-wide spot ($1/e$ level, 2σ as verified using a beam profiler BeamOn-UV, Duma Optronics) on an optical quality surface of a quasimonocrystalline graphite (UPV-1TMO trademark, mass density of 2.25 g/cm^3) sample (dimensions of 10 × 10 × 1 mm^3), mounted inside a plastic cuvette (for optional laser irradiation of samples in liquid environments) on a three-dimensional motorized, PC-driven microstage (Fig. 1). Laser pulse energies were varied and monitored by means of a reflective polarizing attenuator (Avesta Project Ltd.) and a pyroelectric energy meter (OPHIR), respectively. In this work, nanostructuring of a dry graphite surface was performed in ambient air at moderate $E \approx 0.75$ mJ and peak laser fluences $F \approx 0.1$ J/cm^2 (below the single-shot melting and ablation thresholds of graphite, 0.13 and 0.2 J/cm^2,[18–20] respectively) via raster scanning of the sample surface at the velocity $|\boldsymbol{v}| \approx 6$ μm/s. The nanostructured line

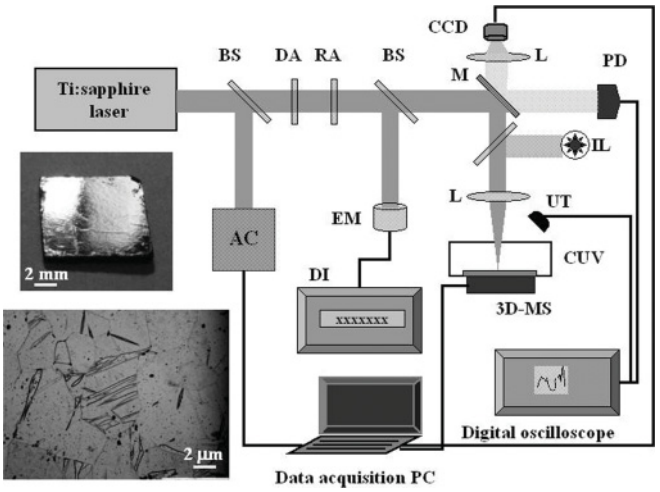

FIG. 1. Experimental setup for fs-laser surface nanostructuring: BS, beam splitter; AC, autocorrelator, DI, digital indicator; DA,RA, variable diffractive and reflective energy attenuators; EM, thermocouple energy meter; M, mirror; L, focusing silica lenses; CCD, charge-coupled device camera for surface imaging; PD, fast trigger silicon photodiode; IL, illumination lamp; UT, ultrasonic transducer; CUV-plastic cuvette with the graphite sample for optional dry or wet nanostructuring; 3D-MS, three-dimensional motorized microstage. Insets: optical camera and microscope images of the HOPG piece.

spots were characterized by means of a scanning electron microscope (SEM) (Quanta FEG 600) at a spatial resolution up to 250 000× via a collection of secondary emitted electrons (the relief SEM mode).

Transient optical constants of the photoexcited graphite during the pumping/SPP excitation stage were studied in a single-shot mode on fresh surface spots by measuring nearly normal ($\approx 9^0$) reflection of the pumping fs-laser pulses with variable pulse energies and deconvolving the reflectivity over the laser spot to obtain the corresponding fluence dependence $R(9^0, F)$.[21]

III. EXPERIMENTAL RESULTS AND DISCUSSION

A. Near-threshold fabrication of multiperiod subwavelength surface gratings

The graphite nanostructures obtained for $F \approx 0.1$ J/cm^2 and the number of shots per spot $N \approx 200$ demonstrate a set of well-defined quasiperiodic nanogratings (the predominating period $\Lambda \approx 200$ nm) with their wave vectors $\boldsymbol{k}_{||}(|\boldsymbol{k}_{||}| = 2\pi/\Lambda)$ collinear to the polarization $\boldsymbol{e}$ and scanning velocity $\boldsymbol{v}$ [Fig. 2(a)]. The orientation of the nanogratings ($\boldsymbol{k}_{||}||\boldsymbol{e}$) is consistent with the standard "interference" model of their fabrication via constructive interference between the incident fs-laser and excited SPP wave.[22,23] It should be noted that though the used relief SEM mode does not provide a surface relief map directly (comparing, e.g., to atomic force microscopy), its map of secondary-electron emission is very sensitive to corresponding relief details yielded in some linear or nonlinear relationships between these two types of surface maps. As a result, such SEM mapping provides a qualitatively adequate Fourier spectrum of a surface relief with the only

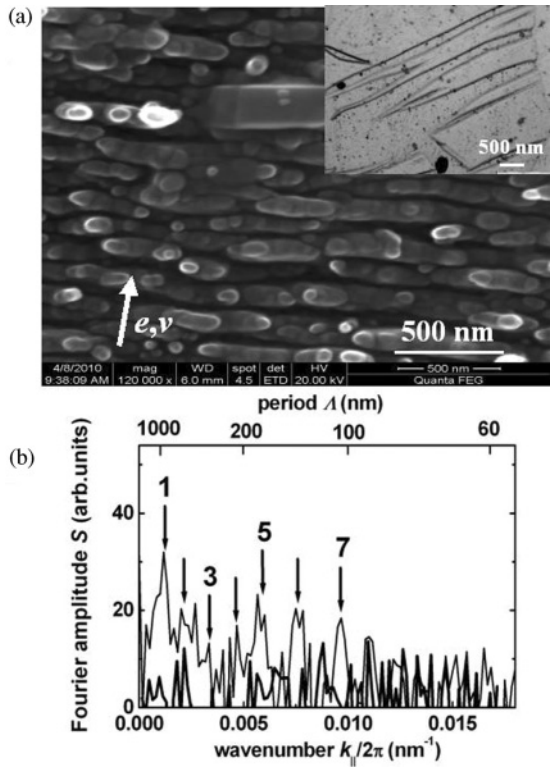

FIG. 2. (a) Top-view SEM image of nanostructures written on the graphite surface at $F = 0.1\,\mathrm{J/cm^2}$ and $N = 200$. The arrow in (a) shows the direction of the laser polarization $\boldsymbol{e}$ and scanning velocity $\boldsymbol{v}$. Inset: optical micrograph of non-irradiated HOPG surface at slightly lower magnification. (b) Amplitude FFT spectra $S(k_{||}/2\pi)$ of the surface nanorelief in (a) in the directions along (thin curve) and across (thick reference curve, representing the noise level) the vector $\boldsymbol{e}$. The arrows show the positions of the higher relief harmonics (m = 1–7), while the top axis shows their corresponding periods.

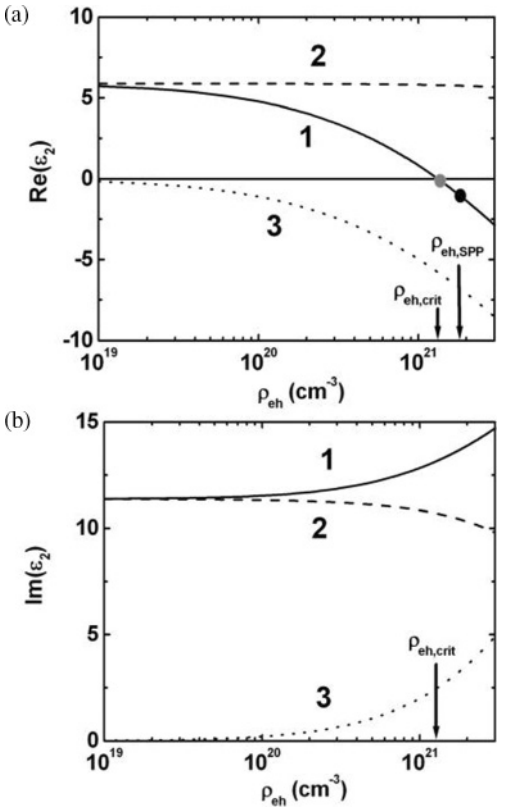

FIG. 3. Real part $\mathrm{Re}(\varepsilon_2)$ (a) and imaginary part $\mathrm{Im}(\varepsilon_2)$ (b) of the dielectric function of photoexcited graphite (solid curve 1) at $\lambda = 744$ nm vs ρ_{eh} with the contribution of interband transitions (dashed curve 2) and the Drude contribution of electron-hole plasma (dotted curve 3). The gray and dark gray circles in (a) correspond to the bulk plasma resonance [the zero-crossing point for $\mathrm{Re}(\varepsilon_2)$] and SPP excitation thresholds at $\rho_{\mathrm{eh,crit}} \approx 1.3 \times 10^{21}\mathrm{cm}^{-3}$ and $\rho_{\mathrm{eh,SPP}} \approx 1.9 \times 10^{21}\mathrm{cm}^{-3}$, respectively.

uncertainty in quantitative amplitudes of its present spatial harmonics.

More detailed topological analysis via one- or two-dimensional fast Fourier transform (FFT) procedure shows a distinct 1D orientation of the nanorelief with the presence of multiple superimposed higher spatial harmonics (m = 1–7) corresponding to wave numbers $|\boldsymbol{k}_{||}|/2\pi = 0.0012$–$0.0084\ \mathrm{nm}^{-1}$ [Fig. 2(b)], while the spatial features corresponding to these harmonics are indeed present in the SEM image. Despite the qualitative SEM representation of the surface nanorelief, the 2DFFT-derived amplitudes of the higher harmonics reasonably decrease in a monotonic manner versus m. To our knowledge, such high harmonics ($m > 2$) were not observed in previous studies (see, e.g., Refs. 4 and 14) also employing the common SEM characterization of surface nanolief, but without the succeding FFT analysis. Furthermore, the corresponding nanogratings with the periods $\Lambda \approx 110$–800 nm (m = 1–7) [Fig. 2(b)] were observed earlier only as separate nanopatterns or their small groups (separate 70-, 120-, or 170-nm gratings, or their series centered near 200 and 120 nm),[12] and, thus, these previous data were not illustrative enough to assign unambigously these nanopatterns as high spatial harmonics.

B. Transient optical constants of fs-laser excited graphite: Threshold for SPP excitation and nanostructuring

Since unexcited graphite exhibits a semiconductor-like character at the optical frequencies because of the predominating interband transitions (Fig. 3), there is a threshold density of the fs-laser excited electron-hole plasma (EHP), $\rho_{\mathrm{eh,SPP}}$, for exciting on the initial planar graphite surface a primary SPP wave with a wavelength Λ_{SPP}, according to the following conditions for the dielectric function of the ambient air and photoexcited graphite, $\varepsilon_1 \approx 1$ and ε_2, respectively:[24]

$$\Lambda_{\mathrm{SPP}} = \lambda_{\mathrm{las}}\mathrm{Re}\left(\sqrt{\frac{\varepsilon_1+\varepsilon_2}{\varepsilon_1\varepsilon_2}}\right), \quad \mathrm{Re}(\varepsilon_1)+\mathrm{Re}(\varepsilon_2) < 0, \quad \mathrm{Re}(\varepsilon_1)\mathrm{Re}(\varepsilon_2) < 0. \tag{1}$$

The existence of such an SPP excitation threshold dictates a threshold-like appearance of such intermediate near-wavelength SPP-driven surface nanoripples at the position of the surface SPP-laser interference maxima via highly localized surface ablation (once the deposited energy density in the maxima exceeds the ablation one) well below the "macroscopic"

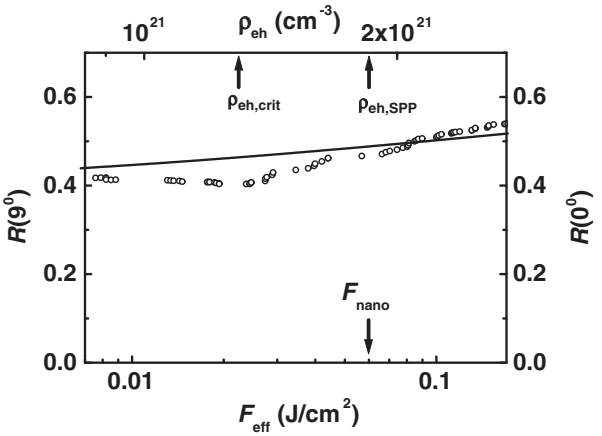

FIG. 4. Experimental dependence (light circles) of the nearly normal-incidence reflectivity $R(9^0)$ of the 744-nm femtosecond laser pump pulses from graphite surface vs effective fluence $F_{\text{eff}} = [1 - R(9^0, F)]F$ (left and bottom axes) in comparison with the calculated one $R(0^0)$ (solid curve) plotted as a function of EHP density ρ_{eh} (right and top axes). The nanostructuring fluence $F_{\text{nano}} = 0.06\text{J/cm}^2$ and the corresponding EHP density $\rho_{\text{eh,nano}} \approx 1.9 \times 10^{21}\text{cm}^{-3}$ are shown by the arrows. The nonlinearity of the F_{eff} and ρ_{eh} scales is dictated by Auger recombination in the dense plasma for $\rho_{\text{eh}} \sim 10^{21}\text{cm}^{-3}$.

graphite ablation threshold $\approx$0.2 J/cm^2 (i.e., the threshold for ablation of the entire graphite surface irradiated for $F >$ 0.2 J/cm^2),[18–20,25] which was indeed observed previously by means of mass spectroscopy of primary ions at 800-nm fs-laser fluences ($\approx$0.1 J/cm^2).[20,25]

To evaluate the SPP excitation threshold density $\rho_{\text{eh,SPP}}$ and the corresponding lower bound value of the nanostructuring threshold F_{nano}, transient optical constants of the photoexcited graphite were probed by studying its slightly oblique ($\approx 9^0$) optical reflection of the 70-fs laser pump pulses in a single-shot mode and the fluence range $F \approx$ 0.01–0.3 J/cm^2, which covers the employed nanostructuring fluence range too. The experimental reflectivity curve $R(9^0, F_{\text{eff}})$ (Fig. 4, bottom axis) demonstrates for $F \approx 0.04$ J/cm^2 ($F_{\text{eff}} = [1 - R(9^0, F)]F \approx 0.025\text{J/cm}^2$) a small dip accompanied by a subsequent reflectivity rise. According to the previous studies, such a dip represents a significant change of the optical constants due to the EHP excitation in the surface layer of the thickness $1/\alpha(744\text{ nm}) \approx 30$ nm [where the absorption coefficient $\alpha(744\text{ nm}) \approx 3.2 \times 10^5\text{cm}^{-1}$ (Ref. 26)] when its density-dependent "bulk" plasma frequency passes over the laser frequency [$\omega_{\text{plas}}^2 = (e^2/\varepsilon_0 m_{\text{opt}})\rho_{\text{eh}} \approx \text{Re}(\varepsilon_{2\text{inter}})\omega_{\text{las}}^2$] at the critical EHP density $\rho_{\text{eh,crit}}$.[18,27]

In order to gain the corresponding EHP density values ρ_{eh}, theoretical modeling of normal-incidence graphite reflectivity $R(0^0)$ at 744 nm was performed as a function of ρ_{eh} for the typical parameters of graphite.[26,28] In these calculations, the dielectric function ε_2 of the photoexcited graphite was taken, as usually, as a sum of interband [Re,Im($\varepsilon_{2\text{inter}}$)] and intraband (Drude) contributions (Fig. 3). The former was acquired from Ref. 26 for the given ω_{las} and the latter was expressed as a common function of ρ_{eh}-dependent plasma frequency ω_{plas} and dephasing time τ [27]

$$\varepsilon_2(\omega_{\text{las}}, \rho_{\text{eh}}) = \left[\text{Re}[\varepsilon_{2\text{inter}}(\omega_{\text{las}}, \rho_{\text{eh}})] - \frac{\omega_{\text{plas}}(\rho_{\text{eh}})^2 \tau(\rho_{\text{eh}})^2}{1 + \omega_{\text{las}}^2 \tau(\rho_{\text{eh}})^2}\right] + \left[\text{Im}[\varepsilon_{2\text{inter}}(\omega_{\text{las}}, \rho_{\text{eh}})] + i\frac{\omega_{\text{plas}}(\rho_{\text{eh}})^2 \tau(\rho_{\text{eh}})}{\omega_{\text{las}}\left[1 + \omega_{\text{las}}^2 \tau(\rho_{\text{eh}})^2\right]}\right], \quad (2)$$

where $\varepsilon_{2\text{inter}}$ becomes a function of ρ_{eh} because of immediate electronic many-body (screening, correlation) effects resulting in ultrafast bandgap renormalization.[29,30] In this work the bandgap shrinkage was accounted for as a model linear positive contribution to the laser frequency,[30] $\Delta\omega_{\text{las}} = \Theta\rho_{\text{eh}}$, where the prefactor Θ was estimated to be equal to 4 eV/4 $\times 10^{22}$ cm^{-3} [compare, e.g., with the same prefactor $\approx$ 0.95 eV/10^{22} cm^{-3} for Te.[30] The latter assumes instantaneous half-shrinkage of the most relevant bandgap $E_M(V_{4-}, V_{3+} \rightarrow C_{3+,4-}) \approx 4$ eV in M-point of the first Brillouin zone[28] upon the optical fs-laser excitation of 10% (i.e., $\rho_{\text{eh}} \approx 4 \times 10^{22}\text{cm}^{-3}$) of the total electron density about $4 \times 10^{23}\text{cm}^{-3}$ in graphite (see GaAs and Te as other examples in Refs. 29 and 30). The "optical" mass $m_{\text{opt}} = m_e m_h/(m_e + m_h) \approx 0.024$ for the ω_{plas} calculation was derived using the effective carrier masses $m_{e,K} = 0.06$ and $m_{h,K} = 0.04$ in K-point from Ref. 28, while its correction for the linear band dispersion—farther from the K-point, closer to the M-point—by the factor of $[1 + (\rho_{\text{eh}}/2.5 \times 10^{23}\text{cm}^{-3})^{1/2}]$ was made using, as the relevant scaling factors, their density-of-state masses. The corresponding masses were extracted from the corresponding electronic density-of-states (e-DOS) distributions[28] $g_{e,h} \propto m_{e,h}^{3/2}$ ascribing all their variations in this narrow region of the Brillouin zone presumably to the variations of $m_{e,h}$. The dephasing time dependence on ρ_{eh} was taken in the empirical form $\tau(\rho_{\text{eh}}) \approx 1$ fs $\times (1 \times 10^{21}\text{cm}^{-3}/\rho_{\text{eh}})^{1/3}$ following the 3D electron gas model[31] and the dephasing time magnitudes presented in Refs. 27, 32– 33.

In lieu of all these used approximations, the calculated dependence $R(0^0, \rho_{\text{eh}})$ (Fig. 4, top axis) provides a reasonable fit to the experimental reflectivity curve with the initial flat region and the following rise, representing a damped plasmon resonance,[27] though the experimental curve exhibits the pronounced change of its slope at $F_{\text{eff}} \approx 0.02\text{J/cm}^2$. The general correspondence of these curves shows that the reflectivity dip and related "dielectric-metal" transition at $\omega_{\text{plas}}(\rho_{\text{eh}}) \approx \text{Re}(\varepsilon_{2\text{inter}})^{1/2}\omega_{\text{las}}$ occurs for the dispersion-corrected optical mass $m_{\text{opt}} \approx 0.10$, approximately, at $\rho_{\text{eh,plas}} \approx 1.3 \times 10^{21}\text{cm}^{-3}$. Similarly, the calculated Re(ε_2) magnitude turns to negative values for $\rho_{\text{eh}} \geqslant 1.3 \times 10^{21}\text{cm}^{-3}$ [Fig. 3(a)], while the SPP excitation threshold condition $\text{Re}(\varepsilon_1) \leqslant -\text{Re}(\varepsilon_2)$ in Eq. (1), according to this figure, is fulfilled for expectedly higher $\rho_{\text{eh,SPP}} \geqslant 1.9 \times 10^{21}\text{cm}^{-3}$.

Importantly, the surface nanostructuring conditions of the present work [$F_{\text{nano}} \approx F_{\text{eff}} \approx 0.06\text{J/cm}^2$($F \approx 0.1\text{J/cm}^2$)] correspond to the EHP density $\rho_{\text{eh}} \approx 1.9 \times 10^{21}\text{cm}^{-3}$ (Fig. 4), which is in good agreement with the above-mentioned SPP excitation threshold $\rho_{\text{eh,SPP}} \approx 1.9 \times 10^{21}\text{cm}^{-3}$. This indicates that in this work, the surface nanostructuring of graphite occurred under near-threshold experimental conditions (obviously, the laser fluence threshold for the initial SPP excitation can be considered as a lower bound for the corresponding

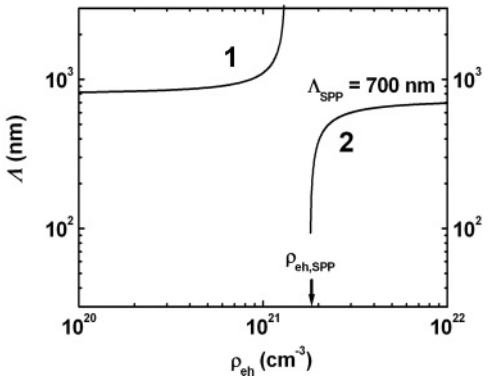

FIG. 5. Calculated SPP-wavelength Λ for the photoexcited graphite surface, vs ρ_{eh}. The branch 1 is unphysical [$\mathrm{Re}(\varepsilon_1) + \mathrm{Re}(\varepsilon_2) > 0, \mathrm{Re}(\varepsilon_1)\mathrm{Re}(\varepsilon_2) > 0$] compared to the branch 2 [$\mathrm{Re}(\varepsilon_1) + \mathrm{Re}(\varepsilon_2) < 0, \mathrm{Re}(\varepsilon_1)\mathrm{Re}(\varepsilon_2) < 0$]. The mark show the SPP excitation threshold $\rho_{eh,SPP} \approx 1.9 \times 10^{21}$ cm^{-3} and the most probable SPP wavelength $\Lambda_{SPP} \approx 700$ nm.

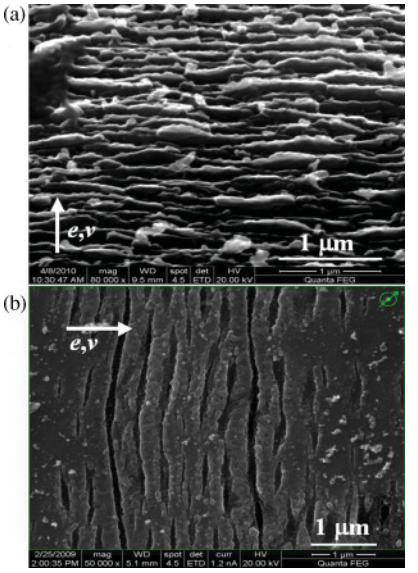

FIG. 6. (a) SEM image of exfoliated graphite sheets on graphite surface nanostructured at $F = 0.1\mathrm{J/cm^2}$ and $N = 200$ (imaging angle of 45°); (b) SEM image of narrow trenches (intermediate nanorelief) on titanium surface nanostructured at near-threshold conditions of $F = 0.02$ J/cm^2 and $N = 50$ (imaging angle of 0°). The arrows show the directions of the laser polarization $\boldsymbol{e}$ and scanning velocity $\boldsymbol{v}$.

surface nanostructuring threshold). Furthermore, such agreement between EHP density magnitude $\rho_{eh} \approx 1.9 \times 10^{21}\mathrm{cm^{-3}}$ at F_{nano} and $\rho_{eh,SPP} \approx 2.3 \times 10^{21}\mathrm{cm^{-3}}$ in Fig. 4 enables one to evaluate, using Eq. (1) and data from Fig. 3, the most probable SPP wavelength $\Lambda_{SPP} \approx 700$ nm (Fig. 5). According to the additional inequality conditions to Eq. (1), the branch 1 is unphysical [$\mathrm{Re}(\varepsilon_1) + \mathrm{Re}(\varepsilon_2) > 0, \mathrm{Re}(\varepsilon_1)\mathrm{Re}(\varepsilon_2) > 0$] not supporting SPP excitation, comparing to the branch 2, when these conditions—$\mathrm{Re}(\varepsilon_1) + \mathrm{Re}(\varepsilon_2) < 0, \mathrm{Re}(\varepsilon_1)\mathrm{Re}(\varepsilon_2) < 0$—are fulfilled. The latter branch demonstrates a strong increase of Λ_{SPP} just above the SPP excitation threshold $\rho_{eh,SPP} \approx 2.3 \times 10^{21}\mathrm{cm^{-3}}$, which is interesting for fs-laser nanostructuring, but this regime can be hardly captured experimentally because of strong variations of ρ_{eh} across the commonly used nonrectangular (e.g., Gaussian or sec^2) temporal profiles of fs-laser pulses. The Λ_{SPP} value is consistent with the fundamental harmonic ($m = 1$) wavelength of the final surface nanorelief, $\Lambda_1 \approx 800$ nm, in Fig. 2.

Finally, using the derived $\rho_{eh}(F_{eff})$ dependence (Fig. 4), it is instructive to evaluate an Auger recombination constant γ_A for graphite, which is, to our knowledge, unknown yet, but could be also relevant for graphene. It is assumed that in the intense fs-laser excitation regime, the linear EHP photogeneration is strongly limited ($\alpha_{744} F_{nano}/\hbar\omega_{las} \gg \rho_{eh,SPP}$, where $\hbar$ is the Planck constant), owing to the Auger recombination process,[34] by the fluence-dependent density

$$\rho_{eh}(F_{eff}) = \sqrt[3]{\frac{\alpha(\rho_{eh})}{\gamma_A \hbar\omega_{las}}\left(\frac{F_{eff}}{\tau_{las}}\right)}. \quad (3)$$

Hence, for the above-mentioned magnitudes ω_{las}, τ_{las}, and $\alpha(744\ \mathrm{nm}, \rho_{eh}) \approx \alpha(744\mathrm{nm}) \approx 3.2 \times 10^5\mathrm{cm^{-1}}$ [see Fig. 3(b) for the weak EHP-induced band-gap renormalization effect on $\mathrm{Im}(\varepsilon_{2inter})$], a few data points—$\rho_{eh,crit} \approx 1.3 \times 10^{21}\mathrm{cm^{-3}}$ at $F_{eff} = 0.025\mathrm{J/cm^2}$ and $\rho_{eh,SPP} \approx 1.9 \times 10^{21}\mathrm{cm^{-3}}$ at $F_{nano} \approx 0.06\mathrm{J/cm^2}$—yield for the strongly excited graphite $\gamma_A \approx (1.0 \pm 0.3) \times 10^{-28}\mathrm{cm^6/s}$, which is reasonably closer to corresponding magnitudes for the narrow-gap semiconductor [see, e.g., 0.55-eV InGaAsSb with $\gamma_A \approx 2 \times 10^{-28}\mathrm{cm^6/s}$ (Ref. 35)] than to wide-gap semiconductors Si, GaAs, and InGaN [4×10^{-31} (direct gap of 3 eV),[34] 1×10^{-29} (1.5 eV),[36] and $2 \times 10^{-30}\mathrm{cm^6/s}$ (2.5 eV) (Ref. 37), respectively], according to the zero K-point band gap in unexcited graphite.[28]

The estimated threshold EHP density $\rho_{eh,SPP} \approx 1.9 \times 10^{21}\mathrm{cm^{-3}}$ enables an evaluation of the corresponding deposited energy density in the interference maxima of the incident fs-laser and primary SPP waves, as a key parameter for ablation of graphite during the fs-laser inscription of its surface nanostructures. Surprisingly, this EHP density corresponds to a volume energy density (enthalpy) magnitude on the graphite surface $\Delta h(F_{nano}) = \rho_{eh,SPP} \times \hbar\omega_{las} \approx 5 \times 10^2\mathrm{J/cm^3}(3 \times 10^3\mathrm{J/mole})$, which is two orders of magnitude lower than the near-critical enthalpy of carbon $\Delta h(\mathrm{crit}) \approx 3 \times 10^5$ J/mole,[38] with the latter providing intense fs-laser ablation of the material,[19] for example, even with rather violent exfoliation of separate graphitic sheets (potentially, graphenes) clearly visible at an angle of 45° [Fig. 6(a)]. However, the ratio $\Delta h(\mathrm{crit})/\Delta h(F_{nano})$ shrinks to ≈ 2.7 upon correction on the factor of Auger (nonradiative) recombination, $\alpha_{744} F_{nano} \hbar\omega_{las} \rho_{eh,SPP}^2 \approx 36$, which rapidly—on a time scale $1/(\gamma_A \rho_{eh,SPP}^2) \sim 1$–10 fs—converts the photogenerated e-h pairs during the pump fs-laser pulse via triple recombination e,e,h and e,h,h collisions into single hot carriers transferring their energy further to the lattice.[23] Hence, the balance between the quantities $\Delta h(F_{nano})$ and $\Delta h(\mathrm{crit})$ in the interference maxima may be achieved at the surface nanostructuring fluence $F \approx 0.1\ \mathrm{J/cm^2}$, roughly, for approximately threefold localization of the deposited laser energy (EM field enhancement $E_{loc}/E_0 \sim 1.7$). Using a relationship for cylindrical SPP waves[16] for a rough estimate

$$\frac{E_{loc}}{E_0} = 8\pi^2\left(\frac{D}{\lambda_{las}}\right)^2, \quad (4)$$

such local field enhancement may indeed be expected for hemicylindrical surface nanoridges and similar features with their diameters $D \sim 0.15\lambda_{las}$. Such small-scale nanotrenches with $D \sim 0.1\lambda_{las}$ and sharp ridges can be experimentally observed as an intermediate periodic nanorelief at near-threshold nanostructuring conditions (see, e.g., narrow trenches on a titanium surface nanostructured under near-threshold conditions [Fig. 6(b)]),[13] resulting, as shown below, in the appearance of higher spatial harmonics ($m \sim \Lambda_{SPP}/D$) of the surface nanorelief during its subsequent multishot fs-laser driven evolution.

C. Modeling of near-threshold fabrication of 1D subwavelength multiperiod surface nanogratings

Our experimental data and previous analysis have demonstrated the initial "interference" formation on the graphite surface of the intermediate nanograting with the experimentally measured single-period $\Lambda_1 \approx 800$ nm, which is reasonably close to the calculated SPP period $\Lambda_{SPP} \approx 700$ nm. Within the "interference" (laser-SPP wave interaction) model,[14,22,23] the overall absorbed surface EM intensity along the surface in the x direction can be represented as[14]

$$\Psi(x) = I_{las}(x) + (I_{las} I_{SPP})^{1/2} \sin\left(\frac{2\pi}{\Lambda_{SPP}} x + \phi\right), \qquad (5)$$

accounting for the contributions of the absorbed laser (I_{las}, typically with almost Gaussian surface distribution) and SPP wave (I_{SPP}) intensities, with the initial phase ϕ. It is the second, spatially modulated interference term, rather than the spatially monotonic first one, that provides the formation of an intermediate surface nanograting, once the absorbed (deposited) EM intensity exceeds the ablation threshold. Therefore, the next question is how the subsequent surface nanostructuring proceeds for different laser fluences $F > F_{nano}$, while producing, for the given Gaussian-shaped laser beam, periodic surface nanotrenches with different *fluence-dependent* widths w and heights h at different ratios $F/F_{nano} > 1$. Though the direct relationship between w,h magnitudes and the incident fluence F is not known yet, it is obvious, from the definition of F_{nano}, that for $F/F_{nano} \gg 1$ pronounced surface nanostructures are expected to emerge [Fig. 7(a)], comparing to subtle nanostructures [Fig. 7(c)] [see, e.g., Fig. 6(b) for a real example] in the case of $F/F_{nano} \geqslant 1$. The central point of our consideration here will be the effect of the intermediate near-wavelength, single-period nanograting relief [in most cases possessing a nonsinusoidal profile, see Fig. 6(b)]—via diffraction of the incident laser wave—on the final cumulative surface nanorelief.

It is well known that in the specific case of a resonance harmonic (sinusoidal) grating, the incident laser wave impinging on the grating at a certain angle θ transforms into a diffracted wave propagating along the grating surface as an SPP wave. The corresponding phase-matching condition then reads[16]

$$\boldsymbol{k}_t + n\boldsymbol{q}_g = \boldsymbol{k}_{||}, \qquad (6)$$

where $\boldsymbol{k}_t$ and $\boldsymbol{q}_g$ are the surface projections of the laser wave vector $\boldsymbol{k_0}(|\boldsymbol{k}_t| = |\boldsymbol{k}_0|\sin\theta;)$ and the grating wave vector, respectively, while the number n is the diffraction order. At the normal incidence ($\theta = 0$) and $n = +1$ or -1, Eq. (6) is simplified to $\boldsymbol{k}_{||} = \boldsymbol{q}_g$ describing the diffractive excitation of an SPP wave with a wavelength equal to the grating spacing.

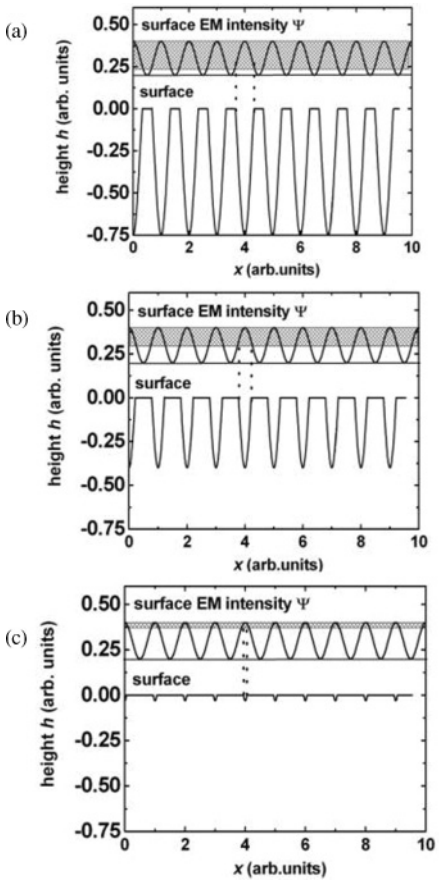

FIG. 7. Truncated, upshifted harmonic model surface profile (bottom curves): truncation level at 75% (a), 40% (b), and 3% (c). The upper curves offset for clarity represent the corresponding surface EM intensity (interference maxima) profiles with the shadow band showing the ablation threshold (the bottom line of the band) and the correspondence between the interference maxima and the ablated surface spots (an example shown by the vertical dotted lines at $x = 4$).

Generally, any rough surface relief can be considered as an infinite set of two-dimensional resonance harmonic gratings with different wave-number pairs $\{\boldsymbol{q}_{gX}, \boldsymbol{q}_{gY}\}$ and heights $S(\boldsymbol{q}_{gX}, \boldsymbol{q}_{gY})$. Then, the different nonsinusoidal (truncated sinusoidal) gratings with the single-period $\Lambda(q_0 = 2\pi/\Lambda)$ and variable nanotrench widths w and heights h appearing in Figs. 7(a)–7(c) at different ratios $F/F_{nano} > 1$ can be represented as corresponding sets of superimposed subwavelength harmonics with the m-folded wave numbers mq_0 [Figs. 8(a)–8(c)]. The subwavelength harmonics spectra are expectedly extending along the $\boldsymbol{q}$ scale versus the decreasing nanotrench width w and height h in terms of the number of the present high-harmonic modes, while their amplitudes are simultaneously decreasing. Particularly, for F values well above the threshold F_{nano} to provide the localized ablation of graphite, but still below the much higher "macroscopic" single-shot ablation threshold for the entire irradiated surface of the corresponding material (0.2 J/cm^2),[18–20] the intermediate single-period nanograting profile is close to that of a resonance

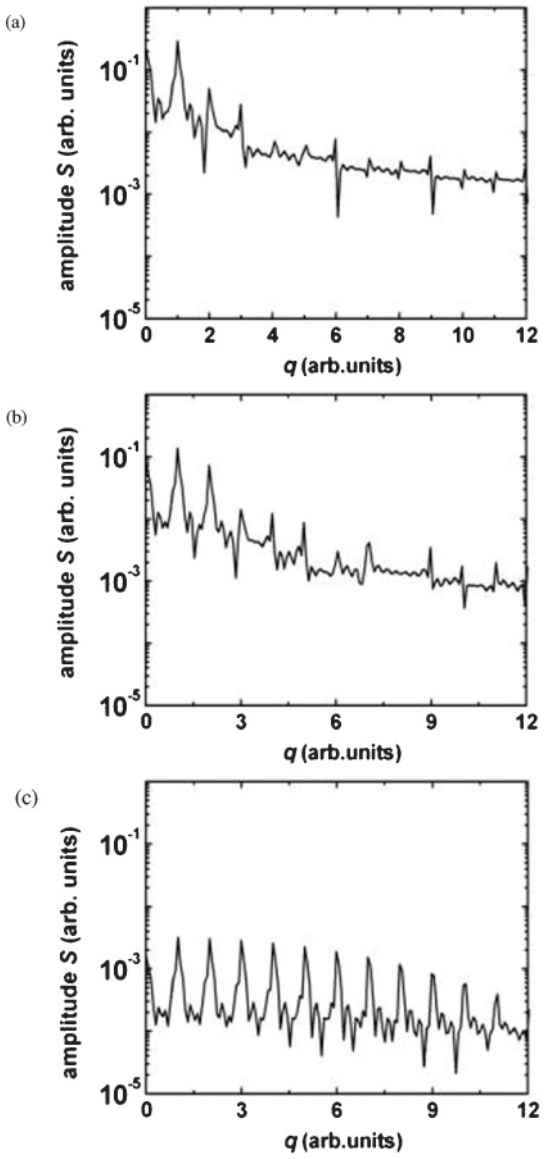

FIG. 8. Amplitude FFT spectra $S(q)$ of the corresponding surface profiles in Fig. 7. The integer magnitudes q represent the orders of the FFT harmonics.

harmonic grating surface [Fig. 7(a)], exhibiting in the FFT spectrum [Fig. 8(a)] almost a single prominent spectral mode and, thus, during laser irradiation tending to the presumable development of the present surface nanograting. In contrast, for the near-threshold $F/F_{\text{nano}} \geqslant 1$, the intermediate single-period surface nanograting possesses minute nanotrench width w and height h [Fig. 7(c)], exhibiting a broad FFT spectrum of low-amplitude high spatial harmonics ($q = mq_0$) [Fig. 8(c)] and providing—via diffraction—excitation of the corresponding low-amplitude, high-q SPP waves with the integer wave numbers mq_0.[16] In the latter case, the constructive interference between the incident laser wave and the excited high-harmonic SPP waves enables surface imprinting of the resulting EM-wave interference patterns in the form of superimposed multiperiod subwavelength nanogratings upon locally exceeding the macroscopic ablation threshold, but for this purpose the low amplitudes of the high-q SPP waves will require cumulative laser irradiation.

We believe this is the case in this work, where the fs-laser nanostructuring of the initially plane graphite surface was performed at the near-threshold conditions ($F/F_{\text{nano}} \geqslant 1$) providing ultranarrow periodic nanotrenches via the above-mentioned "laser-initial SPP wave" interference mechanism. The ongoing diffraction of the incident laser wave on the intermediate anharmonic near-wavelength, single-period surface nanograting seems to provide a number of in-plane diffracted angular components (high-harmonic SPP waves), which are further imprinted—via their constructive interference with the incident laser wave—in each intertrench grating space in the form of superimposed higher nanorelief harmonics.

IV. CONCLUSIONS

In conclusion, in this study, one-dimensional periodical surface nanogratings with a large number of higher relief harmonics (up to 7th order) were written on a flat graphite surface using multiple femtosecond laser pump pulses with fluences slightly above the nanostructuring threshold, and qualitatively visualized by SEM. The observed features of the nanorelief are used to illustrate qualitatively its two-stage formation via fabrication. At the first stage, periodic narrow and broadly spaced nanotrenches (nonsinusoidal relief) occur on the initially flat material surface as a result of interference between electrical fields of the incident femtosecond laser pump pulse and the surface plasmon-polaritonic wave excited via diffraction of the pulse on the seeding surface roughness. At the second stage, diffraction of the incident femtosecond laser pump pulse on the intermediate single-period, near-wavelength nonsinusoidal surface nanograting into a series of in-plane angular components (surface plasmon-polaritonic waves), representing higher harmonics of the intermediate nanograting relief, via their constructive interference with the incident laser wave provides imprinting of the resulting interference maxima in the form of the multiperiod final nanorelief.

ACKNOWLEDGMENTS

This work was partially supported by Russian Foundation for Basic Research (Projects Nos. 08-08-00756a, 09-02-12018-OFI_M, 10-08-00941a, 11-02-01202a, 11-07-00273a, 11-08-01165a, and 11-08-00457a).

*sikudr@sci.lebedev.ru

[1] A. Borowiec and H. K. Hagen, Appl. Phys. Lett. **82**, 4462 (2003).
[2] Q. Wu *et al.*, Appl. Phys. Lett. **82**, 1704 (2003).
[3] T. Q. Jia, H. X. Chen, M. Huang, F. L. Zhao, J. R. Qiu, R. X. Li, Z. Z. Xu, X. K. He, J. Zhang, and H. Kuroda, Phys. Rev. B **72**, 125429 (2005).

[4]J. Bonse, M. Munz, and H. Sturm, J. Appl. Phys. **97**, 013538 (2005).
[5]R. Wagner and J. Gottmann, J. Phys.: Conf. Ser. **59**, 333 (2007).
[6]A. Y. Vorobyev, V. S. Makin, and C. Guo, J. Appl. Phys. **101**, 034903 (2007).
[7]T. Tomita, K. Kinoshita, S. Matsuo, and S. Hashimoto, Appl. Phys. Lett. **90**, 153115 (2007).
[8]Y. Yang, J. Yang, C. Liang, and H. Wang, Opt. Express **16**, 11259 (2008).
[9]G. Miyaji and K. Miyazaki, Opt. Express **16**, 16265 (2008).
[10]J. Bonse, A. Rosenfeld, and J. Kruger, J. Appl. Phys. **106**, 104910 (2009).
[11]S. Sakabe, M. Hashida, S. Tokita, S. Namba, and K. Okamuro, Phys. Rev. B **79**, 033409 (2009).
[12]M. Huang, F. Zhao, Y. Cheng, N. Xu, and Z. Xu, Opt. Express **16**, 19354 (2008); Phys. Rev. B **79**, 125436 (2009).
[13]E. V. Golosov, V. I. Emel'yanov, A. A. Ionin, Yu. R. Kolobov, S. I. Kudryashov, A. E. Ligachev, Yu. N. Novoselov, L. V. Seleznev, and D. V. Sinitsyn, JETP Lett. **90**, 107 (2009).
[14]V. S. Makin, R. S. Makin, A. Y. Vorobyev, and C. Guo, Tech. Phys. Lett. **34**, 387 (2008).
[15]V. S. Makin, Yu. I. Pestov, R. S. Makin, and A. Ya. Vorob'ev, J. Opt. Technol. **76**, 555 (2009).
[16]V. P. Veiko, M. N. Libenson, G. G. Chervyakov, and E. B. Yakovlev, *Laser-Matter Interactions* (Fizmatlit, Moscow, 2008) (in Russian).
[17]V. A. Soifer, Comp. Opt. **32**, 110 (2008) (in Russian).
[18]K. Seibert, G. C. Cho, W. Kutt, H. Kurz, D. H. Reitze, J. I. Dadap, H. Ahn, M. C. Downer, and A. M. Malvezzi, Phys. Rev. B **42**, 2842 (1990); D. H. Reitze, H. Ahn, and M. C. Downer, *ibid.* **45**, 2677 (1992).
[19]K. Sokolowski-Tinten *et al.*, *Femtosecond Laser Induced Ablation of Graphite*, in *Ultrafast Phenomena XI*, edited by T. Elsaesser *et al.*, Springer Series in Chemical Physics, Vol. 66 (Springer, Berlin, 2000), p. 425.
[20]M. Lenner, A. Kaplan, Ch. Huchon, and R. E. Palmer, Phys. Rev. B **79**, 184105 (2009).
[21]S. I. Kudryashov and V. I. Emel'yanov, J. Exp. Theor. Phys. **94**, 94 (2002).
[22]J. E. Sipe, J. F. Young, J. S. Preston, and H. M. van Driel, Phys. Rev. B **27**, 1141 (1983).
[23]S. A. Akhmanov, V. I. Emel'yanov, N. I. Koroteev, and V. N. Seminogov, Usp. Fiz. Nauk **147**, 675 (1985) [Sov. Phys. Usp. **28**, 1084 (1985)].
[24]V. V. Klimov, *Nanoplasmonics* (Fizmatlit, Moscow, 2009) (in Russian); see also the monograph H. Raether, *Surface Plasmons on Smooth and Rough Surfaces and on Gratings* (Springer, Berlin, 1988).
[25]M. Lenner, A. Kaplan, and R. E. Palmer, Appl. Phys. Lett. **90**, 153119 (2007).
[26]*Handbook of Optical Constants of Solids*, edited by E. D. Palik (Academic, Orlando, FL, 1998).
[27]K. Sokolowski-Tinten and D. von der Linde, Phys. Rev. B **61**, 2643 (2000).
[28]R. C. Tatar and S. Rabii, Phys. Rev. B **25**, 4126 (1982).
[29]C. D. Spataru, L. X. Benedict, and S. G. Louie, Phys. Rev. B **69**, 205204 (2004).
[30]S. I. Kudryashov, M. Kandyla, C. A. D. Roeser, and E. Mazur, Phys. Rev. B **75**, 085207 (2007).
[31]See P. C. Becker, H. L. Fragnito, C. H. Brito Cruz, R. L. Fork, J. E. Cunningham, J. E. Henry, and C. V. Shank, Phys. Rev. Lett. **61**, 1647 (1988); J.-Y. Bigot, M. T. Portella, R. W. Schoenlein, J. E. Cunningham, and C.V. Shank, *ibid.* **67**, 636 (1991) for experimental data and theory, respectively.
[32]S. I. Kudryashov, Proc. SPIE **6108**, 61080N (2006).
[33]D. Hulin, M. Combescot, J. Bok, A. Migus, J. Y. Vinet, and A. Antonetti, Phys. Rev. Lett. **52**, 1998 (1984).
[34]C. V. Shank, R. Yen, and C. Hirlimann, Phys. Rev. Lett. **51**, 900 (1983).
[35]S. Anikeev, D. Donetsky, G. Belenky, S. Luryi, C. A. Wang, J. M. Borrego, and G. Nichols, Appl. Phys. Lett. **83**, 3317 (2003).
[36]F. K. Reinhart, J. Appl. Phys. **97**, 123536 (2005).
[37]Y. C. Shen, G. O. Mueller, S. Watanabe, N. F. Gardner, A. Munkholm, and M. R. Krames, Appl. Phys. Lett. **91**, 141101 (2007).
[38]S. I. Kudryashov, Ph.D. thesis, Moscow State University (1999).